

CO line and radio continuum study of elephant trunks: the Pillars of Creation in M16

Yoshiaki Sofue[★]

Institute of Astronomy, The University of Tokyo, Mitaka, Tokyo 181-0015, Japan

Accepted 2020 January 16. Received 2020 January 16; in original form 2019 October 11

ABSTRACT

Molecular line and radio continuum properties of the elephant trunks (ET, Pillars of Creation) in M16 are investigated by analysing $^{12}\text{CO}(J = 1-0)$, $^{13}\text{CO}(J = 1-0)$ and $\text{C}^{18}\text{O}(J = 1-0)$ line survey data from the Nobeyama 45-m telescope and the Galactic plane radio survey at 20 and 90 cm with the Very Large Array. The head clump of Pillar West I is found to be the brightest radio source in M16, showing a thermal spectrum and the properties of a compact H II region, with the nearest O5 star in NGC 6611 being the heating source. The radio pillars have a cometary structure concave to the molecular trunk head, and the surface brightness distribution obeys a simple illumination law from a remote excitation source. The molecular density in the pillar head is estimated to be several $10^4 \text{ H}_2 \text{ cm}^{-3}$ and the molecular mass is $\sim 13\text{--}40 M_{\odot}$. CO-line kinematics reveals random rotation of the clumps in the pillar tail at $\sim 1\text{--}2 \text{ km s}^{-1}$, comparable with the velocity dispersion and estimated Alfvén velocity. It is suggested that the random directions of the velocity gradients would manifest as torsional magnetic oscillation of the clumps around the pillar axis.

Key words: instabilities – stars: formation – H II regions – ISM: molecules – planetary nebulae: general – radio continuum: ISM.

1 INTRODUCTION

Elephant trunks (ET) are cometary dark clouds with head clumps that are supposed to evolve into denser molecular globules to create stars. Typical examples are seen in the H II region M16 in the form of the ‘Pillars of Creation’, widely known from their *Hubble Space Telescope* (HST) images. ETs are considered to be produced by Rayleigh–Taylor instability (RTI) at the interface of an expanding H II region and a molecular cloud (Frieman 1954; Spitzer 1954; Osterbrock 1957; Mackey & Lim 2010), and/or radiation-driven implosion (DRI) caused by the pressure due to photodissociation of the cloud surface by UV photons from O stars (Gritschneider et al. 2010a; Ercolano et al. 2012; Haworth & Harries 2012).

A number of observations of ETs have been obtained from infrared to X rays, particularly extensively in the far-infrared (FIR), in recent decades (Hester et al. 1996; Pilbratt et al. 1998; McCaughrean & Andersen 2002; Carlqvist, Gahm & Kristen 2002; Urquhart et al. 2003; Sugitani et al. 2007; Getman et al. 2012; Hill et al. 2012; Mäkelä, Haikala & Gahm 2017; Pattle et al. 2018; Panwar et al. 2019). See Oliveira (2008) for a review on the ETs in M16 and star formation.

Molecular line observations of the CO lines, which measure the gaseous mass and kinematics directly, have also been obtained in several ETs (Sherwood & Dachs 1976; Schneps, Ho & Barrett 1980;

Gonzalez-Alfonso & Cernicharo 1994; Massi, Brand & Felli 1997; Andersen et al. 2004; Gahm et al. 2006, 2013; Haikala et al. 2017; Mäkelä et al. 2017). Regarding the ETs in M16, several CO-line observations have been obtained (Pound 1998; White et al. 1999; Schuller et al. 2006; Pattle et al. 2018; Xu et al. 2019). In our recent paper on giant elephant trunks (GET) in star-forming spiral arms (Sofue 2019), we provisionally discussed the molecular properties of ETs in M16 as a template. Fig. 1 reproduces the far-infrared (FIR) 8- μm and $^{12}\text{CO}(J = 1-0)$ line intensity maps from Sofue (2019) with the nomenclature used in this article (Pillar East and Pillars West I, II and III), where the data have been extracted from the archival data bases described below.

In this article, we perform a detailed analysis in CO and the radio continuum of the prominent ETs at $l \sim 17^{\circ}.04$ (Pillar East, or the Eagle’s pillar¹) and $l \sim 16^{\circ}.95$ (Pillars West I, II and III, hereafter Pillars I, II and III²). We adopt a distance of M16 of $D = 2.0 \text{ kpc}$ (Hillenbrand et al. 1993; Guarcello et al. 2007).

We utilize the archival CO-line database FOur-beam REceiver System on the 45-m Telescope (FOREST) Unbiased Galactic plane Imaging Survey at Nobeyama (FUGIN; Umemoto et al. 2017³) and the FIR and radio continuum archival data of the Galactic plane

¹<https://apod.nasa.gov/apod/ap181202.html>

²<https://apod.nasa.gov/apod/ap150107.html>

³<http://jvo.nao.ac.jp/portal/nobeyama/fugin.do>

[★] E-mail: sofue@ioa.s.u-tokyo.ac.jp

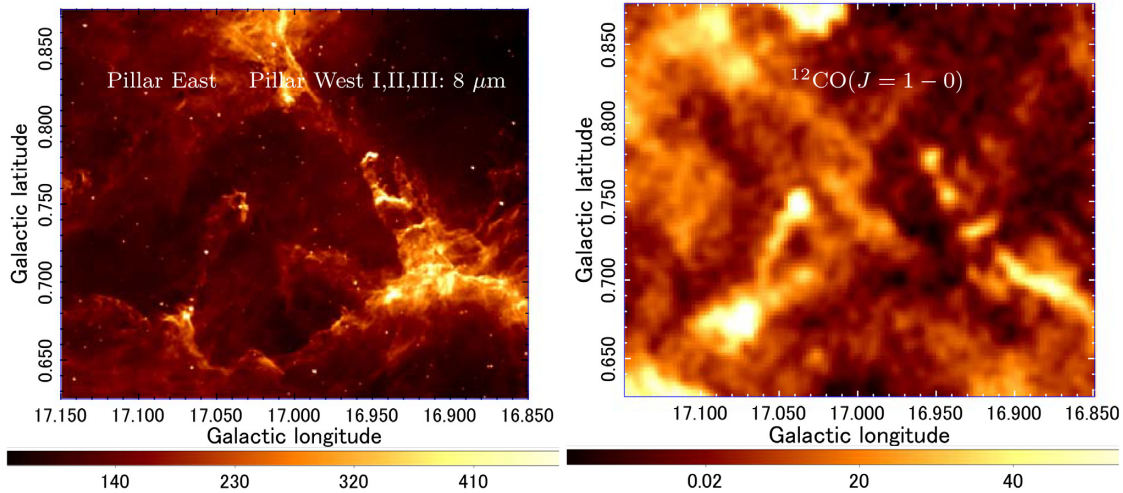


Figure 1. FIR λ 8- μ m map (Jy sr^{-1}), showing PAH (polycyclic aromatic hydrogen) emission from dust-cloud surfaces extracted from MAGPIS and a $^{12}\text{CO}(J=1-0)$ intensity (K km s^{-1}) map of the M16 region. The nomenclature used in this article is indicated: Pillar East and Pillars West (pillars of creation) I, II, III.O

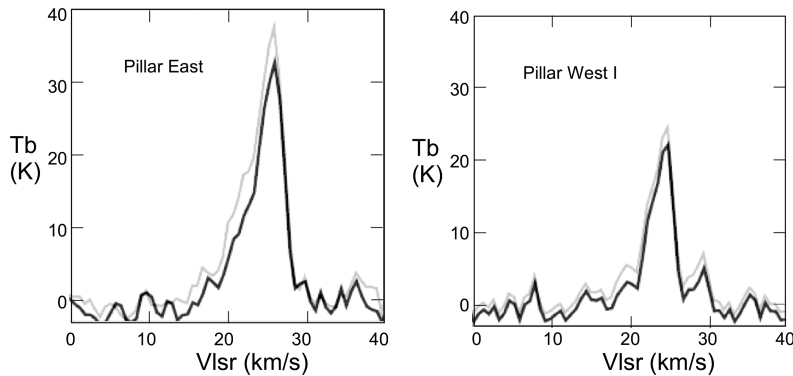


Figure 2. $^{12}\text{CO}(J=1-0)$ line profiles at the molecular tips of Pillars East and West I from $^{12}\text{CO}(J=1-0)$ line emission. Full and grey lines show BGF and original spectra, respectively.

from the Multi-Array Galactic Plane Imaging Survey (MAGPIS; Helfand et al. 2006; Churchwell et al. 2009⁴).

2 DATA AND MAPS

2.1 CO maps

We first present the CO line data of the M16 region in the forms of channel maps, integrated intensity (moment 0), velocity field (moment 1), velocity dispersion (moment 2) maps and longitude–velocity (LV) diagrams. The data were taken from the FUGIN survey (Umemoto et al. 2017). Observations were obtained for the molecular lines of ^{12}CO , ^{13}CO and C^{18}O ($J=1-0$) with full beamwidths at half maximum of 14, 15 and 15 arcsec. The angular resolutions of the resultant maps are 20, 21 and 21 arcsec, respectively, which corresponds to 0.19, 0.20 and 0.20 pc. The velocity resolution was $\Delta v = 1.3 \text{ km s}^{-1}$ and the root-mean-square (rms) noise in the $^{12}\text{CO}(J=1-0)$ line data cube was $\delta T \sim 1.5 \text{ K}$ on average, which yielded noise in the integrated intensity of $\delta I \sim \delta T w \sqrt{w/\Delta v} \sim 3 \text{ K km s}^{-1}$, where $w \sim 4 \text{ km s}^{-1}$ is the line width. The scanning effect in the original data has been

removed by applying the pressing method (Sofue & Reich 1979; Sofue 2019).

Fig. 2 shows the $^{12}\text{CO}(J=1-0)$ line profiles toward the tips of Pillars East and West I. In the analyses below, the diffuse back- and foreground emission has been subtracted from the original maps using the background-filtering (BGF) technique (Sofue & Reich 1979) with a filtering beam of 4.2 arcmin (2.5 pc) in order to measure only the quantities belonging to the pillars.

The line profiles show that Pillar West I has a peak brightness temperature $T_B = 22 \text{ K}$ at radial velocity $v_{\text{LSR}} \sim 24.5 \text{ km s}^{-1}$ and velocity full width $\delta v \sim 3.5 \text{ km s}^{-1}$ (velocity dispersion $\sigma_v \sim 1.8 \text{ km s}^{-1}$), and Pillar East has $T_B = 33 \text{ K}$ at $v_{\text{LSR}} = 25.5 \text{ km s}^{-1}$ with $\delta v \sim 3.6 \text{ km s}^{-1}$.

In the figure, original line profiles without BGF are also shown by grey lines, indicating that 5–10 per cent of the tip emission is due to contamination of the fore- or background extended component. Note that the fractional contamination would be more significant in less intense regions along the pillars.

Figs 3 and 4 show channel maps and integrated intensity maps for v_{LSR} between 20 and 30 km s^{-1} in the M16 region, including Pillars East and West I, II and III, where no BGF has been applied. The ETs are clearly recognized in the $^{12}\text{CO}(J=1-0)$ and $^{13}\text{CO}(J=1-0)$ maps as the two obliquely extended ridges, pointing approximately to the centre of OB cluster NGC 6611 at $(l, b) \sim (16^\circ.95, 0^\circ.8)$.

⁴<https://third.ucllnl.org/gps/index.html>

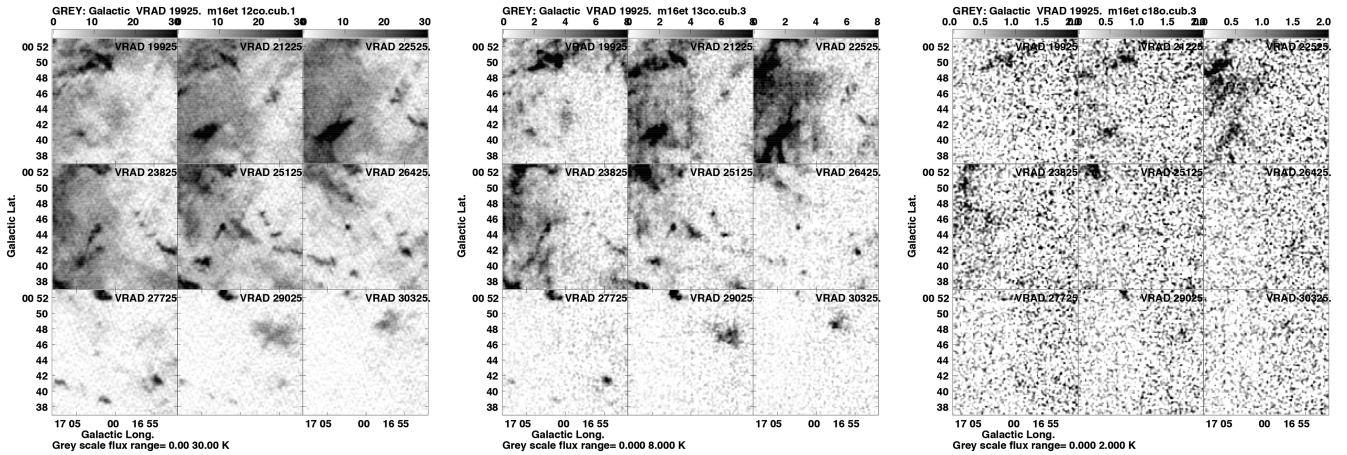


Figure 3. $^{12}\text{CO}(J=1-0)$, $^{13}\text{CO}(J=1-0)$, $\text{C}^{18}\text{O}(J=1-0)$ line channel maps (from right to left) of the M16 elephant trunks region as obtained by the FUGIN CO survey with the Nobeyama 45-m telescope. No BGF is applied. The M16 ETs, or Pillars East and West, show up as two tilted ridges around the centre at position angles $\sim 130^\circ$ and $\sim 45^\circ$, respectively, in channels at $v_{\text{LSR}} \sim 25 \text{ km s}^{-1}$. The greyscale unit is K of T_{B} .

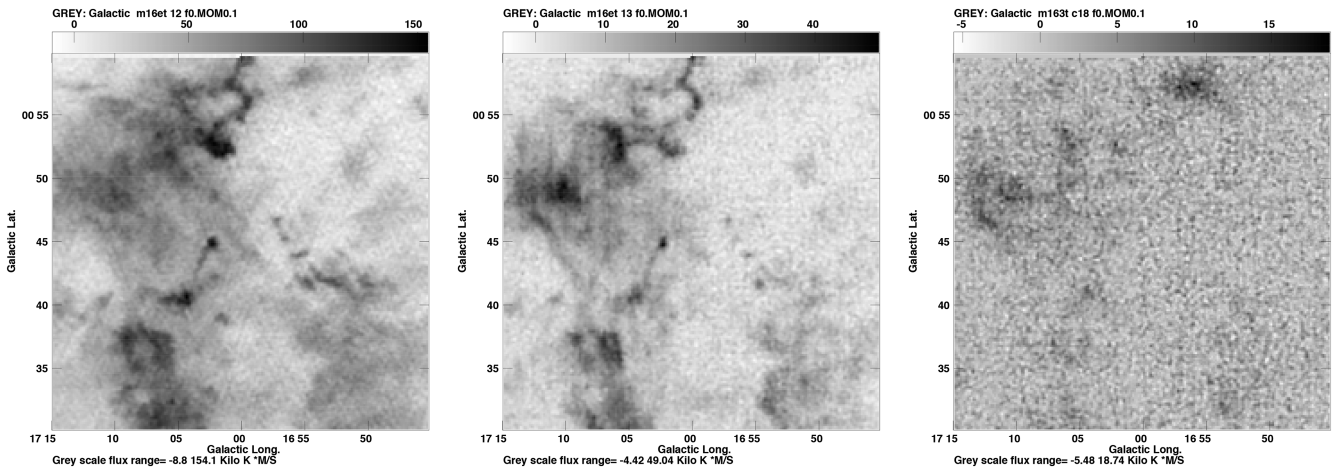


Figure 4. Integrated intensity maps (moment 0) of the $^{12}\text{CO}(J=1-0)$, $^{13}\text{CO}(J=1-0)$ and $\text{C}^{18}\text{O}(J=1-0)$ lines of the M16 elephant trunks region as obtained by the FUGIN CO survey with the Nobeyama 45-m telescope. No BGF is applied. The greyscale unit is K km s^{-1} .

The ETs show up from $v_{\text{LSR}} \sim 23$ to $\sim 27 \text{ km s}^{-1}$, with the centre velocity at 25 km s^{-1} . Fig. 5 shows the velocity field (moment 1) and velocity dispersion (moment 2) in the same region, overlaid with intensity contours.

Fig. 6 shows longitude–velocity (LV) diagrams across Pillars East and West at different latitudes, where the ETs appear as intensity peaks at $l \sim 17^\circ$ and $16^\circ.95$, respectively. The LV ridges show a slight inclination with respect to the vertical axis, showing rotation of the clump around its centre. However, the direction of the inclination at different latitudes (channels) appears not to be uniform, but rather random. A detailed discussion of the rotation of ETs will be given in the last section of this article.

2.2 Radio continuum maps

Fig. 7 shows radio continuum maps at $\lambda 20$ and 90 cm extracted from archival data from MAGPIS for the same region as in Fig. 1. The 20- and 90-cm maps had angular resolutions of $6.2 \times 5.4 \text{ arcsec}^2$ using B, C and D configurations and $24 \times 18 \text{ arcsec}^2$ using B and C configurations, respectively. Note that the upper quarter field is

lacking in the 20-cm map. Since the largest detectable angular scales were 16 and 70 arcmin at 20 and 90 cm, respectively, missing fluxes are negligible in the brightness measurements of the tips of the Pillars.

The 20-cm emission exhibits cometary structures in the radio continuum, coinciding spatially with Pillars East and West I, II and III in FIR and CO line emission. The 90-cm map also reveals the radio pillars, as well as the extended thermal emission from the extended H II region of M16. Radio pillars compose bright head–tail structures coincident with the FIR and molecular ETs.

It is stressed that the radio source at Pillar I’s tip is the brightest compact radio source in the M16 region, which is also coincident with the $8\text{-}\mu\text{m}$ bright spot, although there appears to be a slight displacement between them. Besides Pillars I–III, a broader, but fainter, cometary radio source is associated with Pillar East at $(l, b) \sim (17^\circ.04, 0^\circ.74)$.

In Fig. 8, we show a radio continuum map at 3 cm (10.3 GHz) taken with the Nobeyama 45-m telescope (Handa et al. 1987) in comparison with 20- and 90-cm maps smoothed to the same angular

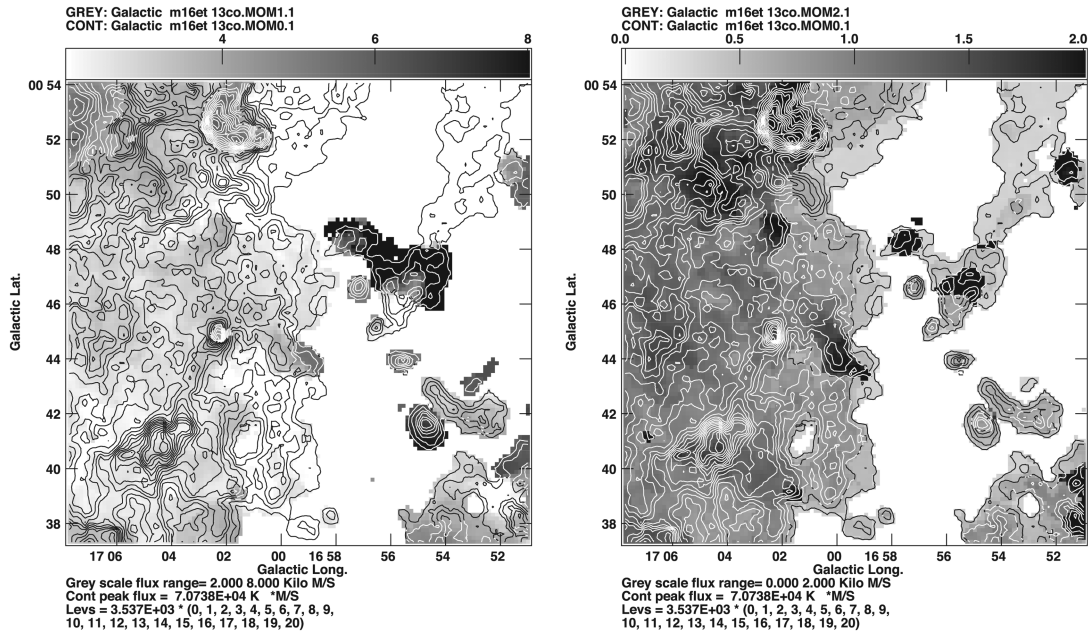


Figure 5. Moment 1 (velocity field) and 2 (velocity dispersion) maps of $^{13}\text{CO}(J=1-0)$ overlaid with moment 0 contours for the central area of Fig. 4. The greyscale unit is km s^{-1} .

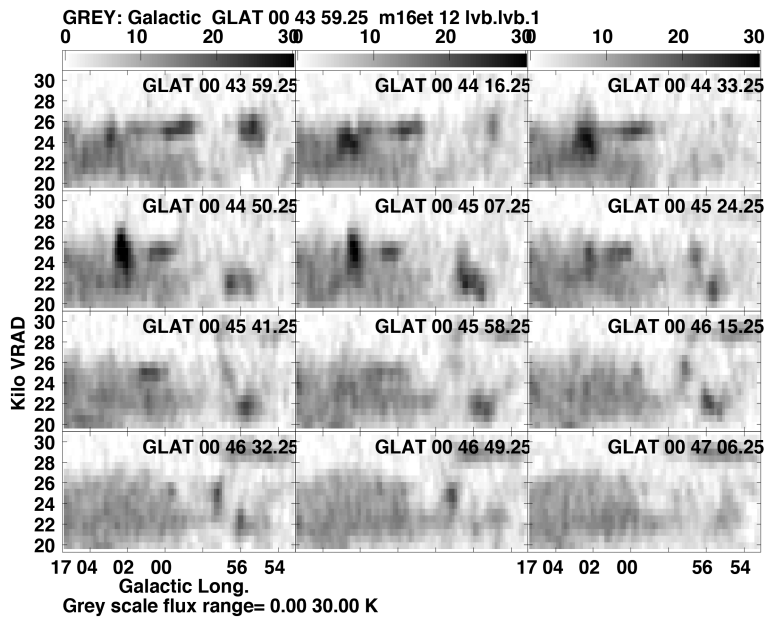


Figure 6. Longitude–velocity (LV) diagrams of $^{12}\text{CO}(J=1-0)$ line emission at different latitudes across ETs East and West at $l \sim 17^\circ 04''$ and $16^\circ 56'–58''$, respectively. The greyscale unit is K in T_B .

resolution as the 3-cm map of 2.6 arcmin. Overlaid contours show the original resolution maps.

3 MOLECULAR PROPERTIES

3.1 Pillars in FIR, CO and radio

In order to investigate the relations between radio continuum, CO line and FIR emission in the pillars in further detail, we enlarge the pillars in Fig. 9. The similarity of the 8- μm and 20-cm radio maps is remarkable. The CO map shows significant displacement of the

peak positions of molecular gas column density from those traced by radio continuum emission. The 90-cm map has lower resolution, while it agrees well with that at 20 cm. A detailed comparison of earlier CO and radio continuum maps with FIR images at various wavelengths has been obtained by White et al. (1999) and Urquhart et al. (2003).

3.2 Molecular Pillars West I, II and III

The $^{12}\text{CO}(J=1-0)$ intensity shows clumpy ridges along the three ETs, with Pillar I being strongest. Using the line profile from the

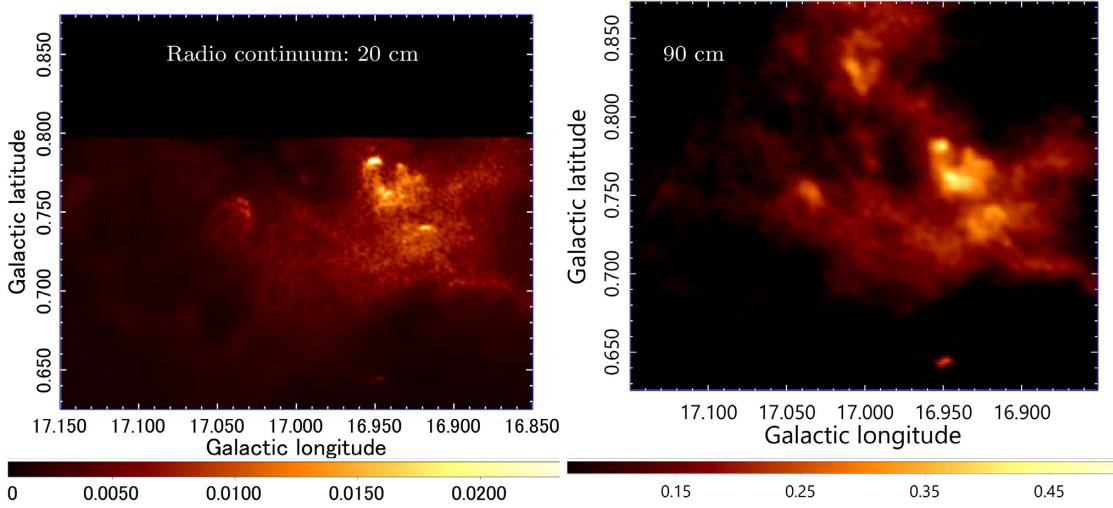


Figure 7. Radio continuum λ 20- and 90-cm maps of the M16 region including the Pillars of Creation in the same region as Fig. 1. Note that the brightest radio source in the region coincides with the tip of Pillar I. Colour bars indicate radio brightness in Jy beam^{-1} .

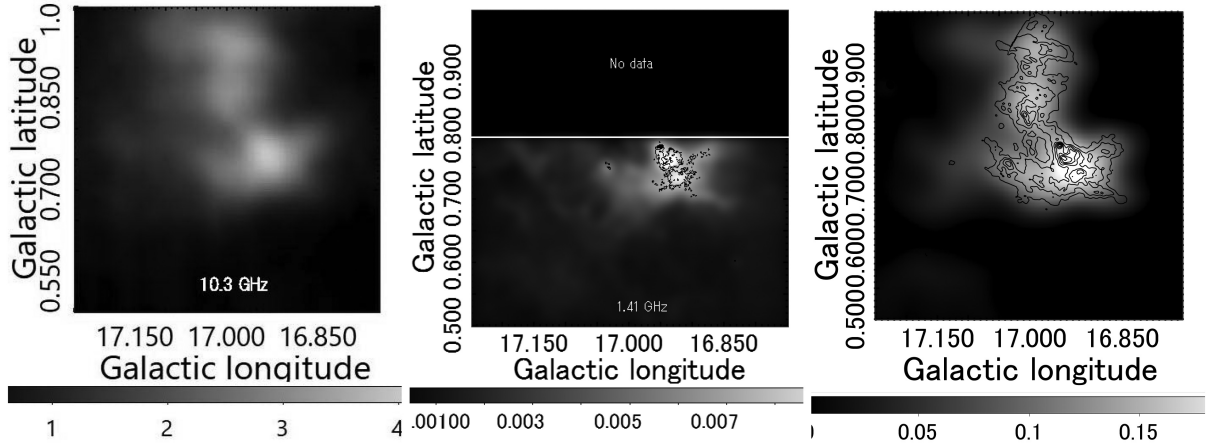


Figure 8. Radio continuum maps of the HII region M16 at 3, 20 and 90 cm smoothed to a beam of 2.6 arcmin (3 cm with 45-m telescope) in greyscales ($\text{Jy}/\text{original telescope beam}$ shown by grayscale bars). Contours indicate the original resolution maps, for reference only.

BGF data cube (Fig. 2), we estimate the integrated intensity to be $I_{\text{CO}} = 77 \simeq T_{\text{B}} \delta v \text{ K km s}^{-1}$, with $T_{\text{B}} = 22 \text{ K}$ and $\delta v = 3.5 \text{ km s}^{-1}$. Applying the CO-to- H_2 conversion factor $X_{\text{CO}} = 2 \times 10^{20} \text{ H}_2 / \text{K km s}^{-1}$ (Bolatto et al. 2013), we obtain a column density of $N_{\text{H}_2} = X_{\text{CO}} I_{\text{CO}} \simeq 1.54 \times 10^{22} \text{ H}_2 \text{ cm}^{-2}$.

The H_2 column can also be calculated by assuming local thermal equilibrium (LTE) of CO molecules in the gas cloud, using both the $^{12}\text{CO}(J=1-0)$ and $^{13}\text{CO}(J=1-0)$ lines. The excitation temperature of the CO molecules is obtained by (Pineda, Caselli & Goodman 2008)

$$T_{\text{ex}} = 5.53194 \times \ln \left(1 + \frac{5.53194}{T_{\text{B}}(^{12}\text{CO}) + 0.83632} \right)^{-1} \quad (1)$$

$$\sim T_{\text{B}} + 3\text{K}. \quad (2)$$

This can be used to estimate the optical depth of the $^{13}\text{CO}(J=1-0)$ line as

$$\tau(^{13}\text{CO}) = -\ln \left(1 - \frac{T_{\text{B}}(^{13}\text{CO})/5.28864}{1/(e^{5.28864/T_{\text{ex}}} - 1) - 0.167667} \right). \quad (3)$$

The column density of ^{13}CO molecules is given by

$$N_{^{13}\text{CO}} = 2.4 \times 10^{14} \frac{\tau T_{\text{ex}}}{1 - e^{-5.28864/T_{\text{ex}}}} \Delta v, \quad (4)$$

which yields the H_2 column by

$$N_{\text{H}_2}(^{13}\text{CO}) = Y_{^{13}\text{CO}} N_{^{13}\text{CO}}, \quad (5)$$

where $Y_{^{13}\text{CO}} = 7.7 \times 10^5$ is the inverse of the abundance ratio of ^{13}CO molecules with respect to H_2 (Kohno et al. 2019).

Inserting the observed peak brightness temperatures of $^{12}\text{CO}(J=1-0)$ and $^{13}\text{CO}(J=1-0)$ lines at the clump head, $T_{\text{B}}(12) = 22 \text{ K}$ and $T_{\text{B}}(13) = 7 \text{ K}$, respectively, and $\Delta v \sim 3.5 \text{ km s}^{-1}$ from the $^{12}\text{CO}(J=1-0)$ line profile, we obtain $N_{\text{H}_2} = 1.61 \times 10^{22} \text{ H}_2 \text{ cm}^{-2}$, in agreement with the estimate from X_{CO} conversion. The present values are consistent with the column density in the Pillars obtained from higher resolution interferometer observations by Pound (1998).

Taking the average of the column densities calculated from the $^{12}\text{CO}(J=1-0)$ intensity with X_{CO} and $^{13}\text{CO}(J=1-0)$ in LTE as $N_{\text{H}_2} = (1.54 + 1.61)/2 \times 10^{22} \simeq 1.6 \times 10^{22} \text{ H}_2 \text{ cm}^{-2}$, the volume density in the head clump of Pillar I is estimated to be $n_{\text{H}_2} =$

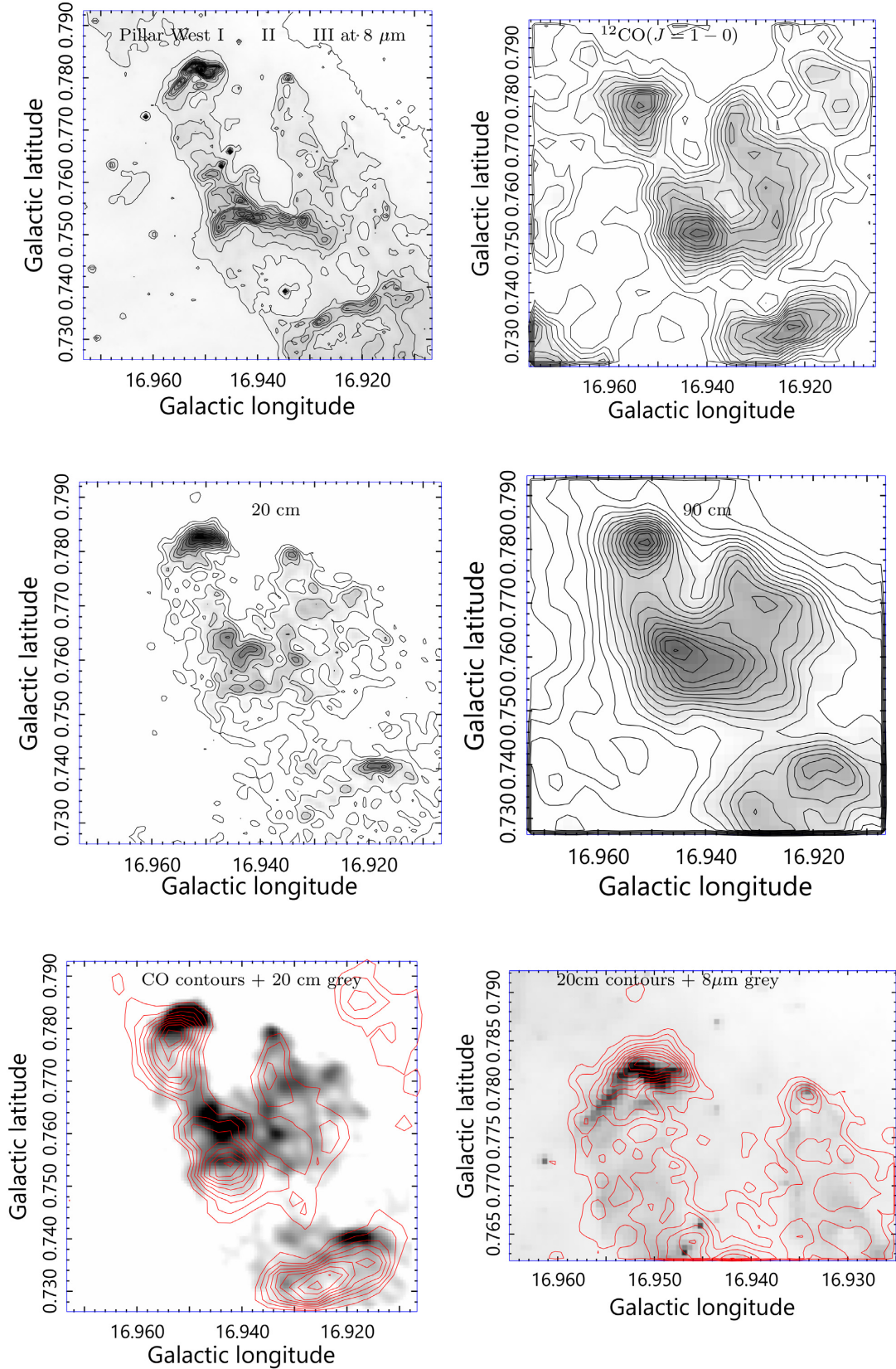


Figure 9. Pillars of Creation I, II and III at 8 μm (contours from 50 at interval of 50 mJy sr^{-1}), $^{12}\text{CO}(J=1-0)$ intensity (contours from 30 K km s^{-1} at interval 5 K km s^{-1}), radio continuum at 20 cm (contours from 0.008 Jy beam^{-1} at interval 0.02 Jy beam^{-1}) and 90 cm (from 0.1 at 0.02 Jy beam^{-1}), CO contours overlaid on 20-cm grey, and 20 cm contours on 8- μm grey. The squared field is $(0^\circ.07 \times 0^\circ.07) = (2.44 \text{ pc} \times 2.44 \text{ pc})$, except for the bottom right panel $(0^\circ.04 \times 0^\circ.03)$.

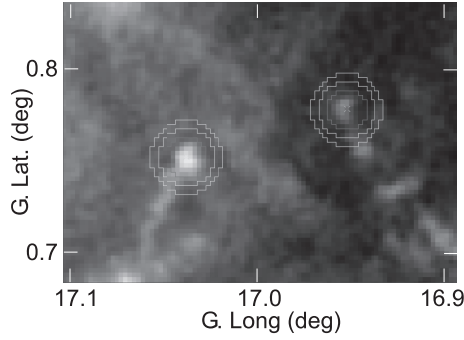


Figure 10. Photometry apertures in order to measure the total molecular masses of the head clumps of Pillars East and West I. The inner circles enclose the objects and the outer two circles enclose the sky to be subtracted.

$N_{\text{H}_2}/d \sim 1.9 \times 10^4 \text{ H}_2 \text{ cm}^{-3}$, where $d = 0.27 \text{ pc}$ is the diameter of the clump in CO emission.

The total molecular mass involved in a sphere of radius $d/2$ is then $M_{\text{mol}} \sim (4\pi/3)(d/2)^3 2.8m_{\text{H}}n_{\text{H}_2} \sim 13.4 M_{\odot}$. The molecular mass was also measured by integrating the observed intensities in the moment 0 map multiplied by the X_{CO} factor, applying an aperture photometry tool to the circles shown in Fig. 10, where the inner circles enclose the sources and the outer two circles enclose the sky to be subtracted. Parameters determined and quantities estimated are summarized in Table 1, where the distance to M16 is assumed to be 2.0 kpc.

The estimated mass of Pillars West I may be compared with the CO($J = 3-2$) line observations by White et al. (1999), who report a molecular mass of $M_{\text{mol}} \sim 60 M_{\odot}$ for Pillar I; an even greater value, $M_{\text{mol}} \sim 300 M_{\odot}$, is reported by interferometer $^{12}\text{CO}(J = 1-0)$ observations (Pound 1998). On the other hand, our result is comparable with those for ETs other than M16. CO observations toward ET clumps in the Rosette Nebula indicate $n_{\text{H}_2} \sim 10^4 \text{ H}_2 \text{ cm}^{-3}$ and $M_{\text{mol}} \sim 6-11 M_{\odot}$ (Schneps et al. 1980) and ETs in four other H II regions of $\sim 6-29 M_{\odot}$ (Gahm et al. 2006).

In order to inspect in more detail the spatial and topological relations between the pillars in CO, radio continuum and $8\text{-}\mu\text{m}$ emission, we show enlarged maps around the head clumps of the pillars in Fig. 9.

The head clumps in the radio continuum are displaced significantly and coherently from those in the $^{12}\text{CO}(J = 1-0)$ line emission, in the sense that radio emission appears to originate on the higher latitude side surfaces of the CO clumps. This trend is also seen in the middle and bottom clumps on the pillars.

On the other hand, the radio head clumps are more closely correlated with the $8\text{-}\mu\text{m}$ clumps, although that in Pillar I is also slightly displaced from $8 \mu\text{m}$ toward the higher latitude direction, in the same sense as against CO.

3.3 Molecular Pillar East

Pillar East is also well known for the *HST* images (Eagle’s Pillar). Fig. 11 shows an enlarged map of the 20-cm brightness around the tip, compared with the $^{12}\text{CO}(J = 1-0)$ and $8\text{-}\mu\text{m}$ maps. The 20-cm map shows a broad cometary structure with a well-defined half

Table 1. Molecular parameters of Pillars West I and East.

	Pillar West I	Pillar East	
Head			
(l, b)	$(16^\circ.96, 0^\circ.78)$	$(17^\circ.04, 0^\circ.75)$	(deg)
v_{LSR}	24.5	25.5	(km s^{-1})
Distance from Sun	2	2	(kpc)
Size parameter, $d = \sqrt{xy}$	0.27	0.36	(pc)
Full velocity width, $\delta v = 2\sigma_v$	3.5	3.6	(km s^{-1})
T_{B}^\dagger of $^{12}\text{CO}(J = 1-0)$	22	33	(K)
T_{B}^\dagger of $^{13}\text{CO}(J = 1-0)$	7	15	(K)
$I_{\text{CO}} \simeq T_{\text{B}}\delta v(^{12}\text{CO}(J = 1-0))$	77	122	(K km s^{-1})
$N_{\text{H}_2}(^{12}\text{CO}(J = 1-0), X_{\text{CO}})$	1.54×10^{22}	2.3×10^{22}	($\text{H}_2 \text{ cm}^{-2}$)
$N_{\text{H}_2}(^{13}\text{CO}(J = 1-0), \text{LTE})$	1.61×10^{22}	2.4×10^{22}	($\text{H}_2 \text{ cm}^{-2}$)
$N_{\text{H}_2}(\text{mean})$	1.6×10^{22}	2.4×10^{22}	($\text{H}_2 \text{ cm}^{-2}$)
n_{H_2}	1.9×10^4	2.3×10^4	($\text{H}_2 \text{ cm}^{-3}$)
M_{mol}^*	13.4	39	(M_{\odot})
$M_{\text{mol}; \text{photo}}^\ddagger$	17.5 ± 0.5	32.6 ± 0.7	(M_{\odot})
Tail			
Length X	~ 6	~ 4	(pc)
Width Y	~ 0.4	~ 0.4	(pc)
$\frac{dv}{dX} \sin i$	$\sim \pm 1$	0.4	($\text{km s}^{-1} \text{ pc}^{-1}$)
$\frac{dv}{dY} \sin i$	$\sim \pm 4$	-0.3	($\text{km s}^{-1} \text{ pc}^{-1}$)
Rotation $\sin i$ at edge	$\sim \pm 0.4$	-0.06	(km s^{-1})
$\langle I_{\text{CO}} \rangle$ of $^{12}\text{CO}(J = 1-0)$	~ 20	~ 30	(K km s^{-1})
$\langle N_{\text{H}_2} \rangle$	$\sim 4 \times 10^{21}$	$\sim 6 \times 10^{21}$	($\text{H}_2 \text{ cm}^{-2}$)
$\langle n_{\text{H}_2} \rangle$	$\sim 3 \times 10^3$	3×10^3	($\text{H}_2 \text{ cm}^{-3}$)
M_{mol}	~ 200	~ 210	(M_{\odot})

Notes. † Diffuse components have been subtracted using the BGF technique.

‡ Photometric value enclosed by the circles in Fig. 10.

* The virial mass is much higher, indicating that the clump is not gravitationally bound (see Section 5.6).

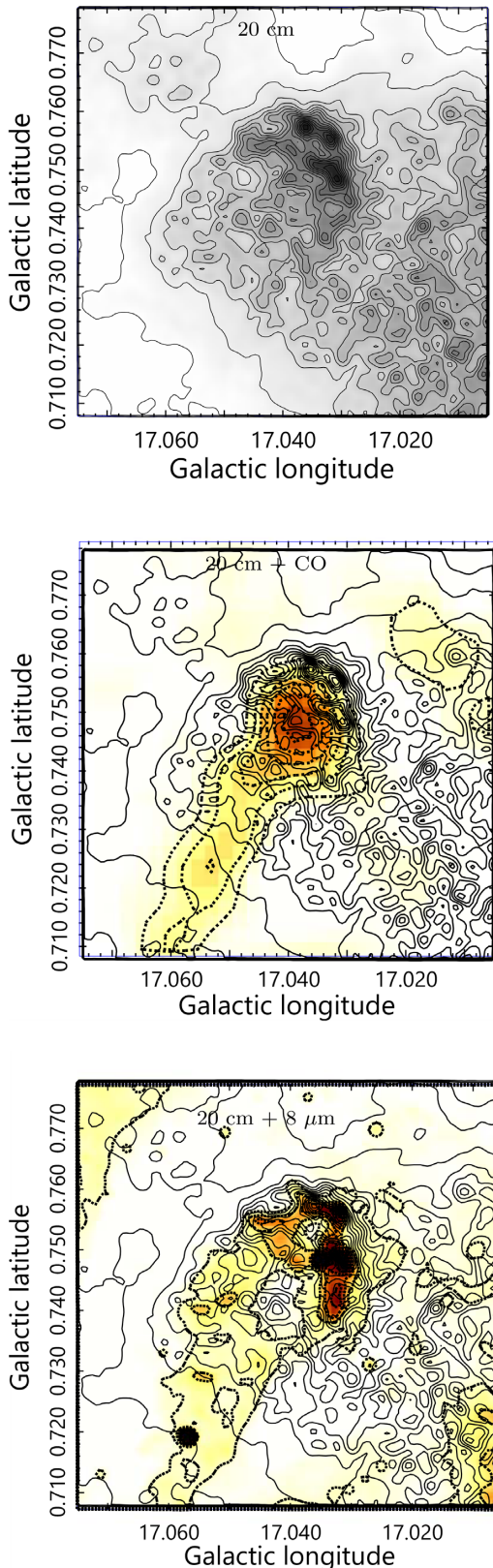


Figure 11. M16 ET East in radio continuum at 20 cm with contours from 0 at $0.01 \text{ Jy beam}^{-1}$ interval, plus overlays on the $^{12}\text{CO}(J=1-0)$ intensity map in grey with dashed contours from 60 at 10 K km s^{-1} interval, and on the $8\text{-}\mu\text{m}$ map with dashed contours from 100 at 10 Jy sr^{-1} . The squared field is $(0^{\circ}07 \times 0^{\circ}07) = (2.44 \text{ pc} \times 2.44 \text{ pc})$.

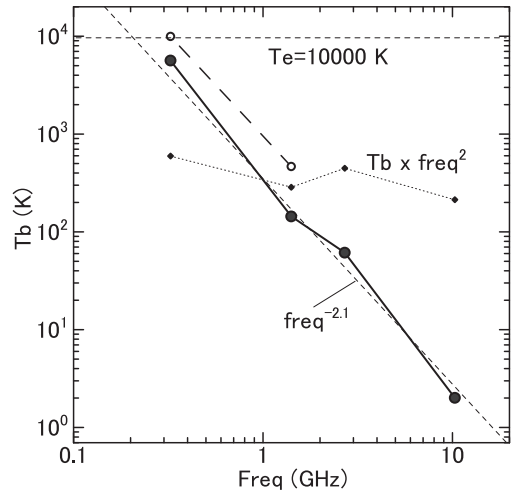


Figure 12. Radio continuum spectrum of Pillar I's peak. Plotted are the peak surface brightness temperatures, T_B , in K at 90, 20, 11 and 3 cm, smoothed to a 3-cm beam (2.6 arcmin), except for 11 cm with the original resolution.

shell surrounding the CO clump. The $8\text{-}\mu\text{m}$ emission also shows a shell feature nearly coincident with the radio shell. The hole at $8 \mu\text{m}$ coincides with the CO intensity peak. Thus, the molecular pillar composes the backbone of the structure, which is enveloped by the FIR, also optical and radio continuum sheaths. The estimated parameters are listed in Table 1.

4 RADIO CONTINUUM PROPERTIES

4.1 Cometary radio cap

The 20-cm continuum map shows that the radio sources at the tips of Pillars East and West I have a cometary cap structure. They are significantly offset from the molecular head clumps and are concave to the centre of the molecular gas distribution. The radio caps coincide spatially with the $8\text{-}\mu\text{m}$ bright rims with a slight offset outward. The radio + CO structure at the heads of the Pillars shows a close resemblance to that observed in bright-rimmed molecular globules associated with conical radio continuum rims produced by photoionization from nearby O stars (Urquhart et al. 2006). Also, our result will prove the current theoretical models, including radiation-driven implosion mechanisms (Haworth & Harries 2012, and the literature therein).

4.2 Thermal radio spectrum

Using the smoothed maps in Fig. 8, we plot a radio continuum spectrum between 10.3 GHz (3 cm) and 0.33 GHz (90 cm) of the head clump of Pillar I in Fig. 12. We also plot the brightness at 2.7 GHz (11 cm) at the original resolution of 4 arcmin from the Bonn 100-m telescope (Reich et al. 1984, 1990). Small open circles show the brightness at the original resolution at 20 and 90 cm.

The radio spectrum is well fitted by that expected for optically thin thermal (free-free) emission with a spectral index of $\beta = -2.1$ ($T_B \propto \nu^\beta$) from ionized gas of an H II region. Since the head clump is nearly resolved in the present Very Large Array (VLA) maps, the brightness temperature at 90 cm at original resolution, $T_B \sim 10^4 \text{ K}$, represents the lower limit on the electron temperature of the brightest spot, which indicates that $T_e \geq 10^4 \text{ K}$, significantly higher

Table 2. Radio continuum properties of the head clump of Pillars West I and East.

Parameter	Pillar West I	Pillar East	
ν	1.41	1.41	(GHz)
T_B	484	172	(K)
T_e (assumed)	10^4	10^4	(K)
τ	0.048	0.017	
EM	3.05×10^5	1.1×10^5	(pc cm ⁻⁶)
$d = \sqrt{xy}$	0.16	0.18	(pc)
n_e	1.36×10^3	0.8×10^3	(cm ⁻³)
M_{HII}	0.07	0.06	(M_\odot)
L_{reco}	487	244	(L_\odot)
Dist. to O star	2.0	3.2	(pc)
L_{source}	6×10^5	5×10^5	(L_\odot)

than observed in extended H II regions, which are observed to have $T_e \sim 7000\text{--}8000$ K (Downes et al. 1980). Accordingly, the turnover frequency would be lower than 0.3 GHz, because the spectrum is nearly straight between 0.33 and 10 GHz.

4.3 Radio Pillar West I

We now derive radio continuum parameters for Pillar I's head cap. The 90-cm map shows that the peak brightness temperature is as high as $T_B \simeq 10^4$ K, indicating that the electron temperature is equal to or higher than this value, $T_e \geq 10^4$ K. In the following, we estimate the density of ionized gas assuming $T_e = 10^4$ K.

The brightness temperature at 20 cm at the peak is measured to be $T_B = 484$ K, which is sufficiently smaller than the electron temperature that we may assume the optical depth at 20 cm is small, $\tau = T_B/T_e \sim 0.048 \ll 1$. Inserting this into the relation between the emission measure EM and frequency,

$$\tau = 0.082(T_e/K)^{-1.35}(\nu/\text{GHz})^{-2.1}EM, \quad (6)$$

we obtain the emission measure $EM = 3.05 \times 10^5$ pc cm⁻⁶.

From the 20-cm radio map, the size diameter, d , of the head clump is measured to be $d = \sqrt{xy} \simeq 0.16$ pc, where $x = 0.23$ and $y = 0.12$ pc are the major and minor axial full widths of the emission region. Assuming that the line-of-sight depth of the radio clump is equal to d , we obtain an electron density of $n_e \simeq 1.36 \times 10^3$ cm⁻³. For this density and size, the mass of the ionized gas is of the order of $\sim 0.1 M_\odot$. The electron density is consistent with that obtained by optical spectroscopy by McLeod et al. (2015), who derived maps of electron density and temperature, showing $n_e \sim 1\text{--}2 \times 10^3$ cm⁻³ and $T_e \sim 1\text{--}2 \times 10^4$ K in the pillar tips.

Thus, the radio continuum clump at Pillar I's head can be categorized as a compact H II region of relatively small size. Pillar I in the radio exhibits approximately the same size, similar cometary morphology, an order of magnitude less EM and several times less electron density, compared with the values observed in typical compact H II regions (Deharveng & Maucherat 1978; Woodward, Helfer & Pipher 1985).

Given the electron density, we may estimate the luminosity of the recombination emission from the clump as $L_{reco} \sim \alpha n_e^2 V E_{UV} \sim 487 L_\odot$, where $\alpha \sim 4 \times 10^{-13}$ cm³ s⁻¹ is the recombination coefficient at $T_e \sim 10^4$ K, $E_{UV} = 13.6$ eV is the ionization energy of neutral hydrogen and $V = 4\pi/3(d/2)^3$ is the volume of the H II region. The radio luminosity due to free-free emission is negligible. The estimated parameters are listed in Table 2.

The recombination time of the clump is therefore as short as $t_{reco} \sim n_e k T_e V / L_{reco} \sim 2$ yr, where k is the Boltzman constant.

Note, however, that this time-scale is a lower limit, because the electron temperature could be higher, as was expected from the high brightness temperature at 90 cm. Equivalently, the cooling time of partially ionized hydrogen gas can be estimated using a cooling rate of $\Lambda \sim 10^{-23}$ erg cm³ s⁻¹ at $T_e \sim 10^4$ K (Foster et al. 2012), which yields $t_{cool} \sim n_e k T_e / (n_e^2 \Lambda) \sim 3$ yr. Thus, the gas must be heated either from the inside or the outside in order to keep its luminosity, if the radio continuum clump is a stable structure.

One of the possible mechanisms of heating for the Pillar I tip is photoionization by UV radiation from stars with effective temperature higher than $\sim 10^4$ K embedded in the H II region. However, there has been no report of such a star or cluster of luminosity comparable to $\sim 487 L_\odot$ in the direction of Pillar I's head (Xu et al. 2019), although there remains a possibility that such stars suffer from heavy extinction and are not recorded in the optical catalogue of Evans et al. (2005), based on which the stellar distribution has been studied. In fact, it is reported that a young stellar object equivalent to a B-type star of several solar masses with $\sim 200 L_\odot$ exists embedded in the molecular tip of Pillar I (McCaughrean & Andersen 2002; Thompson, Smith & Hester 2002), while it is unclear whether the star is luminous enough to maintain the compact H II region.

Another possible mechanism is excitation by UV photons from NGC 6611 about $D \sim 2$ pc away to the Galactic north. Then, the required luminosity of the exciting stars is estimated to be $L_{OB} \sim L_{reco}(4\pi D^2 / [\pi(x/2)^2]) \sim 6 \times 10^5 L_\odot$, which is consistent with the luminosity of two O5 stars in the centre of NGC 6611 (Pound et al. 1998).

4.4 Radio Pillar East

In the same way, the radio properties of Pillar East can be estimated as follows. The brightness temperature is measured to be $T_B \sim 172$ K, which yields an emission measure of $EM \sim 1.2 \times 10^5$ pc cm⁻³. The line-of-sight depth is estimated to be $d \sim 0.18$ pc. We then obtain an electron density of $n_e \sim 0.8 \times 10^3$ cm⁻³. The recombination luminosity is $\sim 244 L_\odot$ and the required luminosity of the exciting stars 3.2 pc away is estimated to be $L_{source} \sim 5 \times 10^5 L_\odot$, consistent with the estimation from the luminosity of Pillar I.

Because of the well-resolved structure in the radio map of Pillar East, we may investigate the intensity distribution in more detail than for Pillar I, which will be useful to clarify the relation to the O stars in NGC 6611 that are supposed to be the UV photon source.

Fig. 13 shows the radio intensity at 20 cm along the surface edge of Pillar East, plotted against the calculated injection-angle parameter defined by $\chi = \sin\theta(D/D_0)^{-2}$. Here, θ is the angle of the pillar's surface as seen from the supposed centre of UV radiation at the O5V star in NGC 6611 and D and D_0 are the distances of the measured point and the tip of the pillar from the star, respectively. Each point indicates a Gaussian-weighted running mean of measured intensities at every 0.1 interval of χ , with a half-width of 0.15. The bars are standard deviations.

The figure shows a linear relation with $\sin\theta$, as expected for illumination from outside. Note that the finite intensity at $\theta \sim 0$ is due to the background emission of the Galaxy. The saturation at $\theta \sim 90^\circ$ is due to smearing by both the finite angular resolution and the intrinsic thickness of the radio shell.

4.5 Radio brightness and distance from exciting star

Besides the dependence on the injection-angle parameter within a pillar, the variation of the peak brightness in different pillars

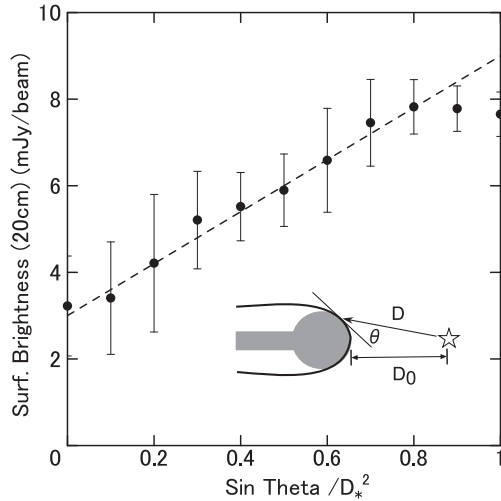


Figure 13. Radio intensity at 20 cm in mJy beam^{-1} along the surface of the cometary H II region of Pillar East against the injection-angle parameter, $\sin \theta / D_*^2$, where $D_* = D/D_0$, with D_0 being the distance of the tip from the centre of NGC 6611. The linear correlation is remarkable. Saturation at $\theta = 90^\circ$ is due to the finite resolution, as well as the intrinsic thickness. The finite value at $\theta \sim 0^\circ$ is due to the Galactic background.

with different distance from the exciting star would be another means to clarify whether the pillars have a common excitation source.

In Fig. 14, we plot the 20-cm peak surface brightness against the projected distance, $D |\sin i|$, of the head clumps of the four pillars discussed in this article from the brightest star of type O5V of NGC 6611. Here, i is the inclination angle of the star–pillar tip line with respect to the line of sight (los), with $i = 0^\circ$ indicating the object on the near-side los. The plot shows that the surface brightness decreases with projected distance, in agreement with the 3D orientation derived from optical spectroscopy and extinction analyses (McLeod et al. 2015).

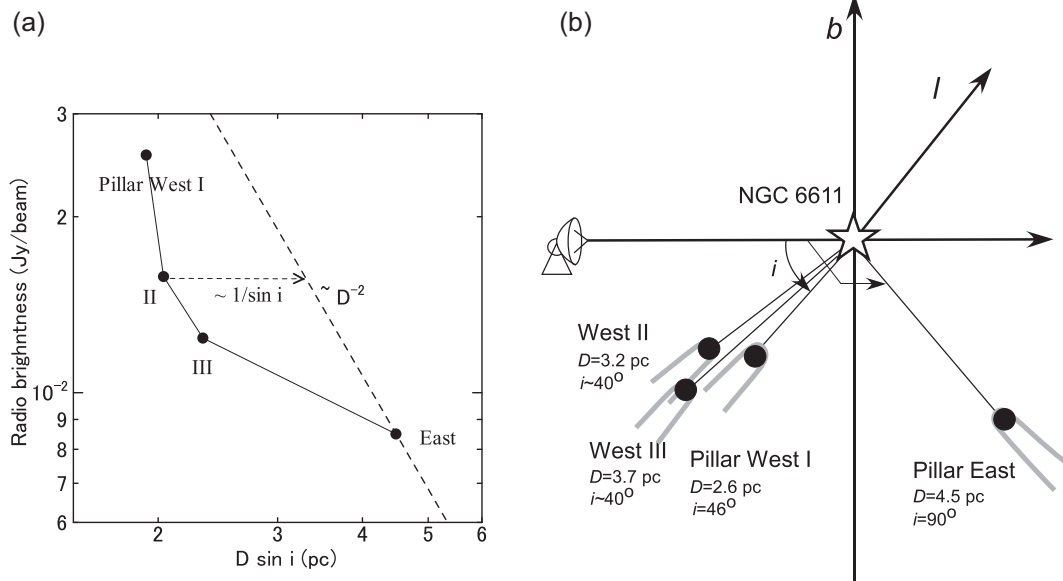


Figure 14. (a) Radio continuum peak brightness at 20 cm of the ET (pillar) heads as a function of the projected distance $D \sin i$ from the brightest O star of NGC 6611. The dotted line shows the relation $\propto D^{-2}$ on an arbitrary scale. (b) 3D positions of the pillars when Pillar East is assumed to have $i = 90^\circ$.

However, the slope of the plot is shallower compared with the inverse-square law for distance. Such a displacement may be attributed either to variable inclinations or to different excitation parameters among the tips. However, the latter may not be the case, because the pillars are formed in the same H II region and their excitation and emission mechanisms would not be so different from one tip to another.

Assuming that the displacement is due to variable inclination, we may derive the 3D orientation of the pillar tips by adjusting i , so that the four tips fall on the D^{-2} line. Because $|\sin i| \leq 1$, Pillar East may be put furthest from the excitation centre, and here we assume $i = 90^\circ$ (in the plane of the sky). Accordingly, the ‘true’ distances of the four tips from the exciting star are assumed to be ~ 2.6 , 3.2, 3.6 and 4.5 pc for West I, II, III and East, respectively. Then Pillars West I, II and III are located at inclinations $i \sim 47^\circ$, 40° and 40° , respectively, while mirror positions with respect to the sky plane are not excluded. Fig. 14(b) illustrates the locations of the pillars with respect to the exciting star at the origin of the coordinates.

We emphasize that the linear relation with the injection-angle parameter in Fig. 13 and the dependence on distance in Fig. 14 prove that heating of the pillars is commonly driven by radiation from the central O stars in NGC 6611.

5 DISCUSSION

5.1 Implosion by H II pressure

Fig. 15 summarizes schematically the spatial relationships between the emission features of the head clump of Pillar I in radio continuum, FIR and CO lines. From such topology, we may draw a scenario to explain the astrophysical processes around Pillar I’s head. In the following order-of-magnitude estimates, we use the projected distances, instead of the distances derived in the previous subsection, allowing for uncertainties of a factor of ~ 2 .

The entire M16 H II region is widely extended and the central part has already been exhausted to compose a cavity around the OB cluster NGC 6611. The pillars are the closest relic of a high-

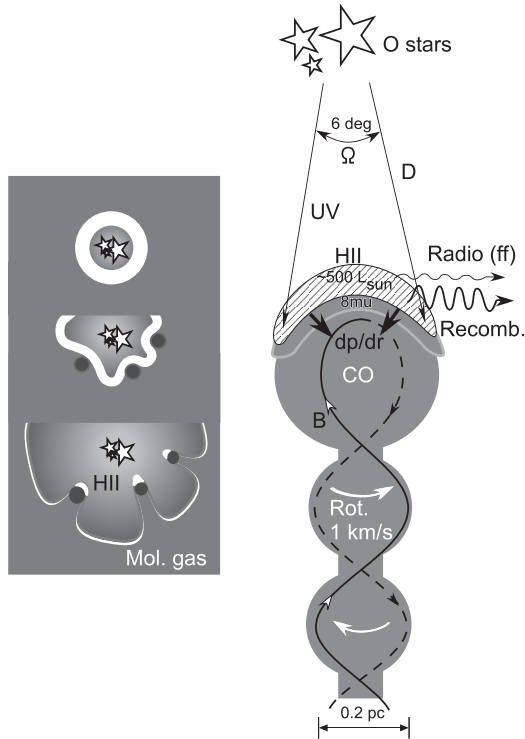


Figure 15. Schematic evolution of elephant trunks in radio continuum and spatial relation between NGC 6611 and Pillar I. UV radiation from the two O5 stars of NGC 6611 of $L_{UV} \sim 7 \times 10^5 L_{\odot}$ in the solid angle of the Pillar I head is comparable to the recombination luminosity of the head clump. The torsional magnetic field will drive rotational oscillation of the clumps.

density molecular clump, where UV photons from O stars are heavily shadowed, so that the pillar tails are protected against dissociation. The strongly illuminated surface of Pillar I’s edge is ionized, and generates a compact H II region with high density and electron temperature, which shines as the brightest radio source in M16.

The compact H II region at the Pillar I tip is concave with respect to the molecular clump, so that the radiation as well as the ionized gas pressure accelerates the molecular surface toward the centre of the clump, leading to implosive compression.

The radiation pressure of UV photons from the O stars of NGC 6611 is of the order of $P_{OB} \sim L_{OB}/(4\pi D^2)/c \sim 1.7 \times 10^{-10} \text{ erg cm}^{-3}$. This pressure is equivalent to the pressure caused by ions expelled from the surface of the neutral gas. On the other hand, the gaseous pressure of the H II gas in the radio cap, when it is maintained there stationary, is $P_{HII} \sim n_e k T_e \sim 1.9 \times 10^{-9} \text{ erg cm}^{-3}$, an order of magnitude more effective than radiation or expelling momentum transfer in order to compress the gas cloud.

These pressures are compared with the thermal pressure and turbulent energy density of the molecular clump, of the order of $P_{mol} \sim 2n_{H_2} k T_{ex} \sim 1.4 \times 10^{-10}$ and $P_{turb} \sim 1/2 \rho \sigma_v^2 \sim 1.5 \times 10^{-9} \text{ erg cm}^{-3}$, where $\rho = 2.8 m_H n_{H_2}$ is the gas density and $\sigma_v \sim 1.8 \text{ km s}^{-1}$ is the velocity dispersion of the gas, which is half the full velocity width.

It is thus found that the external pressure from H II gas is comparable to or slightly higher than the internal pressure of the head clump. Assisted by the concave structure with respect to the cloud centre, it would enhance implosive compression. We point out that the H II pressure is more effective than the radiation pressure from OB stars for implosion, which would give

an observational constraint on the triggering mechanism for star formation in ET heads (Haworth & Harries 2012 and the literature therein).

We here encounter a momentum problem. The total H II mass is only $\sim 0.1 M_{\odot}$, much less than the clump’s molecular mass of $\sim 13 M_{\odot}$. Therefore, the H II cap alone cannot give sufficient momentum to the cloud for contraction, because the H II gas will evaporate within a crossing time of the sound velocity through the cap, $\sim 10^4 \text{ yr}$. In order for the H II cap to act to compress the molecular tip, it must be confined to the pillar by external pressure of the extended H II gas in M16, while the radiation pressure is not enough, as discussed above.

We estimate the emission measure from the brightness of $\sim 0.005 \text{ Jy beam}^{-1}$ at 20 cm near the mid-point between the pillar and NGC 6611 to be of the order of $EM \sim 5 \times 10^3 \text{ pc cm}^{-3}$. If the line-of-sight depth is of the order of $\sim 10 \text{ pc}$ through M16, we obtain $n_e \sim 20 \text{ cm}^{-3}$. Then the electron temperature of the extended H II must be higher than $7 \times 10^5 \text{ K}$, an X-ray temperature, in order to confine the H II cap to the pillar tip; this is, however, not a realistic value. Therefore, we need another mechanism to confine H II gas near the molecular clump. A possible mechanism to confine the H II gas would be a strong magnetic field, as will be discussed in a later section.

5.2 Evolution of pillars

Radio continuum maps reveal an open-cone morphology of the ionized gas, composed of a bright cap of high-density H II gas covering the tip and a cylindrical tail fading away along the molecular pillar. Although such an open cometary structure is often observed in compact H II regions, where the wind from an O star or gas flow associated with expanding gas provides the origin (Reid & Ho 1985), this appears not to be the case for the present pillars. The dynamical pressure due to the wind from O-type stars, the mass-loss rate of which is of the order of $\dot{M} \sim 10^{-5} \text{ yr}^{-1}$ (Markova et al. 2004), is several orders of magnitudes less than the dynamical pressure required to affect the H II region of density $\sim 10^3 \text{ cm}^{-3}$ at the pillar tip. Similarly, gas flow of the expanding H II region around NGC 6611, the density of which is of the order of $\sim 10 \text{ cm}^{-3}$ and expansion velocity $\sim 10 \text{ km s}^{-1}$, is also too weak to affect the pillar’s dynamics.

Along the lines of the currently accepted scenario for the formation of pillars in H II regions, often referred to as the radiation-driven implosion (RDI) mechanism (Schneps et al. 1980; Bertoldi 1989; Whalen & Norman 2008; Gritschneider et al. 2010b; Mackey & Lim 2010; Haworth & Harries 2012), we here consider the formation and evolution of the M16 pillars to be the following (Fig. 15).

When the OB cluster, NGC 6611, was born, the entire M16 region was deeply embedded in a dense molecular cloud. As the H II sphere expands, the molecular wall is pushed to cause Rayleigh–Taylor instability and radiation-driven implosion grows to form a wavy surface with dense cores left behind as the heads of the elephant trunks. The inner surface of the molecular cavity is ionized and a high-density H II shell is produced, which also follows the wavy growth of instability.

As the waves grow, retarded portions of the front evolve into stretched elephant trunks. Accordingly, the UV flux per unit area on the molecular surface becomes highly non-uniform, due to the variation of the injection angle, θ , as well as the distance, D , from the excitation stars.

As an ET grows, the angle on the side wall decreases to $\theta \sim 0^\circ$ or even becomes negative and photodissociation of the surface ceases.

On the other hand, the top of the head clump, which is much closer to the stars, is still strongly illuminated at $\theta \sim 0^\circ$, when the side wall is shadowed. Such a scenario is partly proved by the fact that the radio brightness along the surface of the pillar obeys a simple illumination law, as shown in Fig. 13.

5.3 Rotation

Fig. 6 showed tilts of intensity ridges on the LV diagrams. Such velocity gradients are more clearly seen in the clumps on the tails than in the heads. Fig. 16 shows LV diagrams of the tails of Pillar East at $b \sim 0^\circ.75$ and Pillars I and II at $b = 0^\circ.773$. The velocity gradient is $dv/dl \sim +2 \text{ km s}^{-1}/20 \text{ arcsec} \sim 1.0 \text{ km s}^{-1}/0.1 \text{ pc}$ across the tail of Pillar East, and $\sim -2 \text{ km s}^{-1}/15 \text{ arcsec} \sim 1.4 \text{ km s}^{-1}/0.1 \text{ pc}$ across Pillars I and II.

The velocity gradient may represent either shear motion in an unbound clump or rotation (spin). In the former case, the pillar would be destroyed and disappear in one crossing time, or in $\sim 1 \text{ Myr}$. However, the coherent alignment of the clumps along the pillar indicates that they are long-lived structures, so that the velocity gradient is more naturally understood as due to rotation and spin. If the ETs are rotating at a velocity of $\sim 1\text{--}2 \text{ km s}^{-1}$, the rotation period is $2\pi r \text{ pc}/1.4 \text{ km s}^{-1} \sim 0.6 \text{ Myr}$.

Rotation directions of Pillars I and II are parallel at the same latitude. On the other hand, the spin direction is not systematic along each tail, as shown in the LV channel maps (Fig. 6), where the velocity gradient directions vary with latitude along the pillar. Moreover, the velocity field (moment 1) map in Fig. 5 shows varying gradients in the ETs.

These facts indicate that the rotation (spin) axes of the molecular clumps are random, suggesting that clump rotation originates in clouds with turbulent motion before evolving into ETs. Such random rotation is in contrast to the regulated rotation and helical structure along the elephant trunk in the Rosette Nebula (Carlqvist et al. 2002; Gahm et al. 2006).

5.4 Magnetic field

Pattle et al. (2018) recently performed submillimetre polarimetric measurement of the distribution of directions of the magnetic field projected on the sky in the Pillars and found that the field lines run parallel to the pillar ridges. Applying the Chandrasekhar & Fermi (1953) method and assuming a molecular hydrogen density taken from Pound (1998), they estimated the magnetic strength to be $B \sim 170\text{--}320 \mu\text{G}$ in Pillar II, where the field directions are regulated along the trunk axis with a polarization angle deviation of $\sigma_\theta \sim 14^\circ$.

We here apply the same method to estimate the magnetic strength in Pillar I's head clump by adopting the presently obtained molecular hydrogen density, $n_{\text{H}_2} = 1.9 \times 10^4 \text{ H}_2 \text{ cm}^{-3}$. According to Pattle et al. (2018), the projected field direction in Pillar I is more scattered than in II and may be read as $\sigma_\theta \sim 30^\circ$ from their figure of field directions. The magnetic strength in the Pillar I tip is, then, calculated as

$$B \sim 9.3 \sqrt{n_{\text{H}_2}} \Delta v / \sigma_\theta \sim 180 \mu\text{G}, \quad (7)$$

where $\Delta v = \sigma_v \sqrt{8 \ln 2}$ with $\sigma_v = 1.8 \text{ km s}^{-1}$ and $n_{\text{H}_2} \sim 2 \times 10^4 \text{ H}_2 \text{ cm}^{-3}$.

We also estimate the field strength by assuming equipartition between the turbulent and magnetic energy densities,

$$B \sim \sqrt{4\pi\rho\sigma_v^2} \sim 190 \mu\text{G}, \quad (8)$$

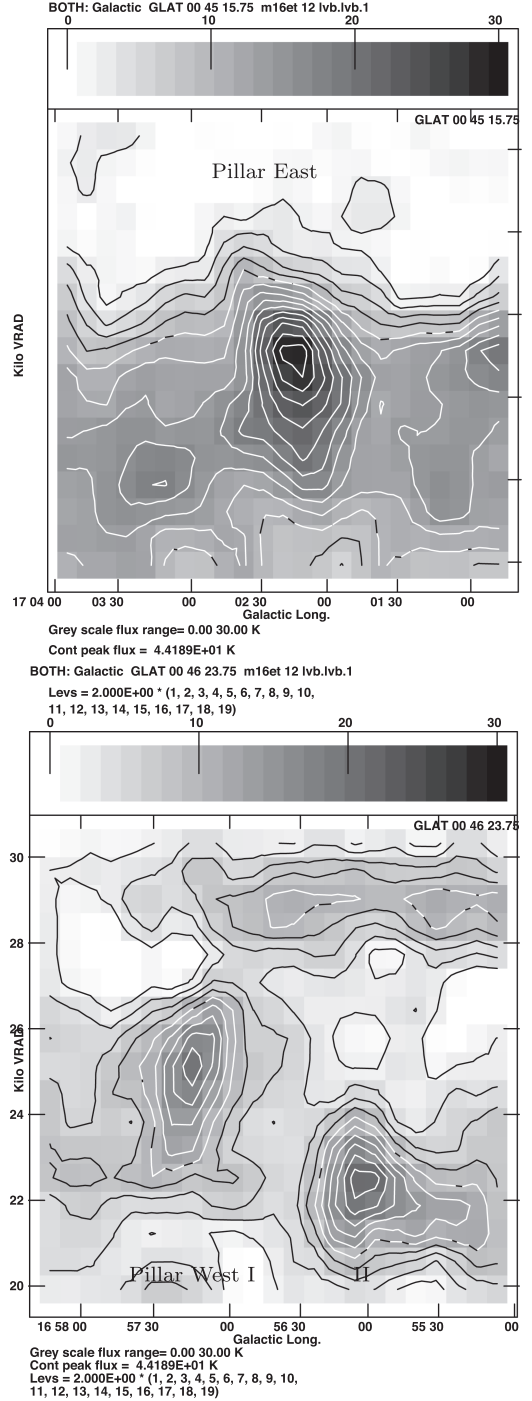


Figure 16. LV diagrams across Pillar East at $b = 0^\circ.754$ and Pillars I and II at $b = 0^\circ.773$, showing the rotation of the trunk tails.

where $\rho = 2.8m_{\text{H}}n_{\text{H}_2}$, consistent with the above estimation. In the same way, the magnetic strength of the Pillar East head is estimated to be $\sim 210 \mu\text{G}$. On the other hand, the field strength in the tail of Pillar I is weaker, $B \sim 72$ and $75 \mu\text{G}$, respectively, for the two methods, according to the lower density $n_{\text{H}_2} \sim 3 \times 10^3 \text{ H}_2 \text{ cm}^{-3}$.

5.5 Torsional magnetic oscillation

Due to magnetic torsion, rotation of the clumps will not be stationary, but may represent a snapshot of spinning oscillation

around the axes, as supported by the fact that the Alfvén velocity is of the same order as the rotation velocity, $V_A = B/\sqrt{4\pi\rho} \sim 1.7$ km s⁻¹, at Pillar I's tip and in the tail.

Pattle et al. (2018) attributed the origin of the regular magnetic structure to tangling of field lines in the parent molecular cloud during the growth of the pillar. This model may be combined with the present observation of random rotation of the clumps. Below, we propose a model of interstellar torsional magnetic oscillation (TMO), as illustrated in Fig. 15. TMO was originally introduced in the study of rotational oscillation of a star by torsional tension due to a twisted magnetic field (Plumpton 1957) and has been applied to axisymmetric magnetic systems (Bisnovatyi-Kogan 2007).

Interstellar TMO occurs in elephant trunks in the following way. The lines of force along the axes of the pillar are twisted by the rotation of the clumps. The rotation is accelerated due to the conservation of angular momentum, as compression proceeds. Accordingly, the magnetic field is amplified, and in turn it produces an expelling force to cause counterrotation. Such motion will result in rotational oscillation of the clumps.

The equation of torsional motion of a clump for rotation angle ϕ can be written as

$$\frac{d^2\phi}{dt^2} = -\frac{B^2}{4\pi\rho r^2}\phi, \quad (9)$$

where the first term is the magnetic tension and the second is the inverse of the specific moment of inertia. Then, the equation is solved to yield

$$\phi = \phi_0 \cos(\omega t - \alpha), \quad (10)$$

where $\omega = V_A/r$ and ϕ_0 and α are constants of integration. The period of oscillation is, therefore, given by $t_{\text{TMO}} = 2\pi/\omega \sim 0.5$ Myr, where $r \sim 1.3$ pc, $B = 180$ μG and $n_{\text{H}_2} \sim 2 \times 10^4$ H₂ cm⁻³, or $V_A \sim 1.7$ km s⁻¹.

5.6 Magnetic confinement of gravitationally unbound clump

In order for the DRI to compress the molecular clump dynamically, the momentum of the H II cap must be greater than, or at least comparable to, that of the molecular clump. For this, the H II masses must be comparable because they are at rest, which is, however, not the case, such that the H II mass is two orders of magnitude smaller than the molecular mass. Also, the external H II region of M16 surrounding the cap does not have sufficient pressure. Hence, some other confinement mechanism is required.

We here propose that the magnetic field of the pillar can act as an effective container of the H II cap. As the conductivity of H II gas is sufficiently high, the gas is almost perfectly frozen into the magnetic field. This means that the H II cap can be confined near the molecular surface by magnetic tension. In fact, the specific magnetic tension, which is of the order of $B^2/4\pi \sim 3 \times 10^{-9}$ erg cm⁻³, is greater than the gaseous pressure in the cap, $n_e k T_e \sim 2 \times 10^{-9}$ erg cm⁻³. Note that this pressure is approximately equal to the dynamical pressure due to velocity dispersion in the molecular clumps.

External compression is also necessary in order for the molecular clumps to be bound against expansion due to velocity dispersion and rotation. In fact, the virial mass is estimated to be $M_{\text{vir}} \sim r\sigma_v^2/G \sim 10^2 M_\odot$ for the observed radius $r \sim 0.14$ – 0.18 pc and velocity dispersion $\sigma_v \sim 1.7$ km s⁻¹ in the tips of Pillars West I and East, which is much greater than the observed molecular masses from CO line measurements (Table 1). Higher virial mass than the mass in the LTE assumption of CO lines has also been reported in another ET clump in M16 (Andersen et al. 2004). Similarly, comparable

or even greater mass is required to bind the clumps gravitationally against centrifugal force by rotation.

Thus, external confinement, such as that due to magnetic pressure and tension, is necessary not only to maintain high pressure of dense ionized gas on the clump's surface, assisting the RDI in working and making the pillar creative in star formation, but also to keep the molecular clump as a bound system. However, there remains a question as to whether such a non-virialized, hence gravitationally stable, clump can be a star-forming site.

6 SUMMARY

We investigated the molecular and radio continuum properties of the elephant trunks, known as the Pillars of Creation, associated with the H II region M16 by analysing archival data of CO line emission from the FUGIN survey with the Nobeyama 45-m telescope and radio continuum survey of the Galactic plane with the VLA.

We showed that the head clump of Pillar I comprises the brightest radio source of thermal (free-free) emission in the entire M16 H II region. The radio source is categorized as a compact H II region of relatively small size and low density for its radio intensity and extent. The head clumps of the other ETs are also found to be strong radio sources. The radio morphology around the ETs is characterized by a cometary structure concave to the molecular trunk head.

Although Pillar I's head is bright in radio emission, no catalogued OB stars exist inside the pillar responsible for heating of the H II gas. Instead, the radio luminosity of the Pillar I head can be explained as due to UV illumination by the nearest O5V star of NGC 6611. The radio intensity distribution around the Pillar East head indicates a linear relation of intensity against injection-angle parameter, proving that the heating source is the same O stars in NGC 6611.

CO line kinematics revealed that the clumps in the pillars are rotating at ~ 1 – 2 km s⁻¹, comparable with the velocity dispersion and Alfvén velocity. The spin directions are random, suggesting that the rotation is a relic of turbulent cloud motion before growth into ETs. We propose an interstellar TMO mechanism to explain the random rotational motion.

ACKNOWLEDGEMENTS

The CO data were taken from the archives of the FUGIN Galactic plane survey using the Nobeyama 45-m telescope. The 8- μm , 20-cm and 90-cm data were extracted from the archival data base MAGPIS (<https://third.ucllnl.org/gps/index.html>). The data analysis was carried out at the Astronomy Data Center of the National Astronomical Observatory of Japan.

REFERENCES

- Andersen M., Knude J., Reipurth B., Castets A., Nyman L. Å., McCaughrean M. J., Heathcote S., 2004, *A&A*, 414, 969
 Bertoldi F., 1989, *ApJ*, 346, 735
 Bisnovatyi-Kogan G. S., 2007, *MNRAS*, 376, 457
 Bolatto A. D., Wolfire M., Leroy A. K., 2013, *ARA&A*, 51, 207
 Carlqvist P., Gahm G. F., Kristen H., 2002, *Ap&SS*, 280, 405
 Chandrasekhar S., Fermi E., 1953, *ApJ*, 118, 113
 Churchwell E. et al., 2009, *PASP*, 121, 213
 Deharveng L., Maucherat M., 1978, *A&A*, 70, 19
 Downes D., Wilson T. L., Bieging J., Wink J., 1980, *A&AS*, 40, 379
 Ercolano B., Dale J. E., Gritschneider M., Westmoquette M., 2012, *MNRAS*, 420, 141
 Evans C. J. et al., 2005, *A&A*, 437, 467

- Foster A. R., Ji L., Smith R. K., Brickhouse N. S., 2012, *ApJ*, 756, 128
- Frieman E. A., 1954, *ApJ*, 120, 18
- Gahm G. F., Carlqvist P., Johansson L. E. B., Nikolić S., 2006, *A&A*, 454, 201
- Gahm G. F., Persson C. M., Mäkelä M. M., Haikala L. K., 2013, *A&A*, 555, A57
- Getman K. V., Feigelson E. D., Sicilia-Aguilar A., Broos P. S., Kuhn M. A., Garmire G. P., 2012, *MNRAS*, 426, 2917
- Gonzalez-Alfonso E., Cernicharo J., 1994, *ApJ*, 430, L125
- Gritschneider M., et al., 2010a, *ApJ*, 723, 971
- Gritschneider M., Burkert A., Naab T., Walch S., 2010b, *ApJ*, 723, 971
- Guarcello M. G., Prisinzano L., Micela G., Damiani F., Peres G., Sciortino S., 2007, *A&A*, 462, 245
- Haikala L. K., Gahm G. F., Grenman T., Mäkelä M. M., Persson C. M., 2017, *A&A*, 602, A61
- Handa T., Sofue Y., Nakai N., Hirabayashi H., Inoue M., 1987, *PASJ*, 39, 709
- Haworth T. J., Harries T. J., 2012, *MNRAS*, 420, 562
- Helfand D. J. et al., 2006, *AJ*, 131, 2525
- Hester J. J. et al., 1996, *AJ*, 111, 2349
- Hill T. et al., 2012, *A&A*, 542, A114
- Hillenbrand L. A., Massey P., Strom S. E., Merrill K. M., 1993, *AJ*, 106, 1906
- Kohno M. et al., 2019, *PASJ*, submitted
- Mackey J., Lim A. J., 2010, *MNRAS*, 403, 714
- Mäkelä M. M., Haikala L. K., Gahm G. F., 2017, *A&A*, 605, A82
- Markova N., Puls J., Repolust T., Markov H., 2004, *A&A*, 413, 693
- Massi F., Brand J., Felli M., 1997, *A&A*, 320, 972
- McCaughrean M. J., Andersen M., 2002, *A&A*, 389, 513
- McLeod A. F. et al., 2015, *MNRAS*, 450, 1057
- Oliveira J. M., 2008, *Handbook of Star Forming Regions, Volume II*, ASP monograp. p. 599
- Osterbrock D. E., 1957, *ApJ*, 125, 622
- Panwar N., Samal M. R., Pandey A. K., Singh H. P., Sharma S., 2019, *AJ*, 157, 112
- Pattle K. et al., 2018, *ApJ*, 860, L6
- Pilbratt G. L., Altieri B., Blommaert J. A. D. L., Fridlund C. V. M., Tauber J. A., Kessler M. F., 1998, *A&A*, 333, L9
- Pineda J. E., Caselli P., Goodman A. A., 2008, *ApJ*, 679, 481
- Plumpton C., 1957, *ApJ*, 125, 494
- Pound M. W., 1998, *ApJ*, 493, L113
- Reich W., Fuerst E., Haslam C. G. T., Steffen P., Reif K., 1984, *A&AS*, 58, 197
- Reich W., Fuerst E., Reich P., Reif K., 1990, *A&AS*, 85, 633
- Reid M. J., Ho P. T. P., 1985, *ApJ*, 288, L17
- Schneps M. H., Ho P. T. P., Barrett A. H., 1980, *ApJ*, 240, 84
- Schuller F. et al., 2006, *A&A*, 454, L87
- Sherwood W. A., Dachs J., 1976, *A&A*, 48, 187
- Sofue Y., 2019, *PASJ*, in press
- Sofue Y., Reich W., 1979, *A&AS*, 38, 251
- Sofue Y. et al., 2018, *PASJ*
- Spir L., Jr, 1954, *ApJ*, 120, 1
- Sugitani K. et al., 2007, *PASJ*, 59, 507
- Thompson R. I., Smith B. A., Hester J. J., 2002, *ApJ*, 570, 749
- Umamoto T. et al., 2017, *PASJ*, 69, 78
- Urquhart J. S., White G. J., Pilbratt G. L., Fridlund C. V. M., 2003, *A&A*, 409, 193
- Urquhart J. S., Thompson M. A., Morgan L. K., White G. J., 2006, *A&A*, 450, 625
- Whalen D. J., Norman M. L., 2008, *ApJ*, 672, 287
- White G. J. et al., 1999, *A&A*, 342, 233
- Woodward C. E., Helfer H. L., Pipher J. L., 1985, *A&A*, 147, 84
- Xu J.-L. et al., 2019, *A&A*, 627, A27
- Zhu F.-Y., Zhu Q.-F., Li J., Zhang J.-S., Wang J.-Z., 2015, *ApJ*, 812, 87

This paper has been typeset from a $\text{\TeX}/\text{\LaTeX}$ file prepared by the author.